Published in final edited form as:
*Inhal Toxicol*. 2012 December ; 24(14): 995–1008. doi:10.3109/08958378.2012.745633.

# NLRP3 inflammasome activation in murine alveolar macrophages and related lung pathology is associated with MWCNT nickel contamination

**Raymond F. Hamilton Jr.**[1], **Mary Buford**[1], **Chengcheng Xiang**[2], **Nianqiang Wu**[2], and **Andrij Holian**[1]

[1]Center for Environmental Health Sciences, University of Montana, Missoula, Montana, USA

[2]Department of Mechanical and Aerospace Engineering, West Virginia University, Morgantown, West Virginia, USA

## Abstract

Multi-walled carbon nanotubes (MWCNT) have been reported to cause lung pathologies in multiple studies. However, the mechanism responsible for the bioactivity has not been determined. This study used nine different well-characterized MWCNT and examined the outcomes *in vitro* and *in vivo*. MWCNT, from a variety of sources that differed primarily in overall purity and metal contaminants, were examined for their effects *in vitro* (toxicity and NLRP3 inflammasome activation using primary alveolar macrophages isolated from C57Bl/6 mice). In addition, *in vivo* exposures were conducted to determine the inflammatory and pathogenic potency. The particles produced a differential magnitude of responses, both *in vivo* and *in vitro*, that was associated most strongly with nickel contamination on the particle. Furthermore, the mechanism of action for the Ni-contaminated particles was in their ability to disrupt macrophage phagolysosomes, which resulted in NLRP3 activation and subsequent cytokine release associated with prolonged inflammation and lung pathology.

### Keywords

Inflammasome; multi-walled carbon nanotubes; nickel; macrophage; NLRP3

## Introduction

With the rapid development of nanotechnology, engineered nanomaterials (ENM), which typically fall into the size range of 1–100 nm in at least one dimension, are receiving intense interest (Li et al., 2011). Nanospheres and one-dimensional nanostructures (nanowires, nanorods, nanobelts, and nanotubes), which are the prevailing forms of ENM (Wang et al., 2008), exhibit different physical and chemical properties from similar bulk or micron-sized



*Address for Correspondence*: Andrij Holian, Center for Environmental Health Sciences, 32 Campus Dr.—Skaggs 280, University of Montana, Missoula, MT, 59812, USA. Tel.: (406) 243–4018; Fax: (406) 243–2807. andrij.holian@mso.umt.edu.

Declaration of interest
The authors report no declaration of interest.

material (Wu et al., 2005, 2010), offering new or improved engineered applications and medical uses (Lanone & Boczkowski, 2006; Liang et al., 2008). For example, semiconducting nanospheres and nanowires exhibit a quantum confinement effect as their diameter is reduced below a critical value (the Bohr Radius) (Davis & Swanson, 2010; Wang et al., 2010). For instance, the catalytic activity of particles is dramatically different as the particle size decreases to nanometer scale (Poizot et al., 2000). According to an analytical study by RNCOS (2009), the global market for nanotechnologies is projected to grow at an annual rate of 20% till 2013 and the market for products incorporating emerging nanotechnology will be worth $1.6 Trillion. Unfortunately, the prospects of inadvertent exposures will likely increase with increased production and use. Therefore, concern has been raised regarding the potential health effects of these new nanomaterials.

Complicating the concerns of potential exposures is insufficient information on what characteristics of ENM result in the greatest health risk. Questions remain regarding the potential of certain ENM to cause chronic inflammation leading to lung granulomas and/or fibrosis as reported in animal models (Lam et al., 2006; Qu et al., 2009; Mercer et al., 2010; Warheit et al., 2004; Shvedova et al., 2005). Furthermore, discrepancies in study outcomes for the same class of materials (e.g. multi-walled carbon nanotubes (MWCNT)) make the risk assessment more difficult. There is a wide discrepancy in the *in vitro* cytotoxicity of MWCNT reported in a number of studies (Lewinski et al., 2008). Likewise, *in vivo* studies report variable outcomes for MWCNT exposures in animal models (Johnston et al., 2010). Variations in the manufacturing methods of these materials provide one possible explanation for the inconsistent results presented in the literature. For example, MWCNT are prepared by a variety of methods using different metals as catalysts and the contents of residual catalysts are different even when the same catalysts are used. This variability in manufacturing results in differences in the size, structure, and metal content of carbon nanotubes (Lam et al., 2006). Metallic particles have been proposed to initiate lung and systemic inflammation by various mechanisms including oxidant stress and activation of the NLRP3 inflammasome (Nel et al., 2006; Martinon et al., 2009).

MWCNT cause lung inflammation, leading to lung fibrosis. However, the molecular mechanism of action has not been elucidated. Studies from various laboratories have included cell toxicity, oxidant stress, cytokine production and recently lysosomal disruption and NLRP3 inflammasome activation (Nel et al., 2006; Liu et al., 2007; Hamilton et al., 2009). Well-characterized fibrogenic particles such as silica and asbestos have been shown to activate the NLRP3 inflammasome resulting in the release of potent inflammatory cytokines such as IL-1β and IL-18 that are important in resulting pathogenesis (Dostert et al., 2008). IL-1β and IL-18 are cytokines specifically related to the activation of the NLRP3 inflammasome (Tschopp & Schroder, 2010; Cassel et al., 2009; Drenth & van der Meer, 2006). Recently, Hamilton et al., reported that $TiO_2$ nanobelts activate the NLRP3 inflammasome (Hamilton et al., 2009), consistent with an inflammatory response *in vivo* (Bonner, 2010; Porter et al., 2012). Therefore, the present study used a family of nine related MWCNT that were provided by the National Toxicology Program and characterized by the Research Triangle Institute. The aim of this study is to test the hypothesis that the inflamma-

tory potential of MWCNT is correlated with activation of the NLRP3 inflammasome and is due mainly to variation of residual metal contaminants in the MWCNT.

## Methods

### Characterization of MWCNT

The bulk MWCNT samples were provided to us by Dr Nigel Walker and Brad Collins at the National Toxicology Program (NTP) at the National Institute of Environmental Health Sciences (NIEHS). Procurement and characterization of the bulk unformulated MWCNT were carried out for the NTP by the Research Triangle Institute under NIEHS contract N01-ES-65554. Address information for the suppliers can be found in Table 1. Purity of each MWCNT was analyzed by thermal gravimetric analysis (TGA) with a TA Instruments TGA Q500. 10 mg aliquot of each sample was accurately weighed and transferred to a platinum sample pan and was then subject to TGA analysis. The instrument was gradually ramped to a temperature of 850°C. Duplicate aliquots of each study sample were analyzed.

The metal content in the MWCNT samples was determined by X-ray fluorescence (XRF) spectrometry. 250 mg aliquot of each sample was transferred to an XRF sample cup and sealed with film. Cups were loaded into the Thermo Noran Quantex energy dispersive XRF and were analyzed with filter conditions optimized for determination of Fe, Co, Ni, Mo, and Y. Using these filter conditions, the presence of additional metals present at significant levels would also have been detected. Samples were analyzed in duplicate fashion.

The diameter of the MWCNT samples that were placed on the carbon-coated 400 Mesh copper TEM Grid (Ted Pella, Inc., Redding, CA) was determined by a FEI Tecnai $G^2$ Twin Transmission Electron Microscope (Shared Materials Instrumentation Facility, Duke University). Over 50 representative TEM images were taken and an average of >150 MWCNT was measured for each sample. Fovea Pro software was used for the diameter measurement. The procedure involves threshold adjustment and MWCNT overlap area masking to obtain accurate measurement of the MWCNT diameters. Summary of characterization data can be found in Figure 2.

The zeta potentials of MWCNT samples were determined by the Malvern Zetasizer Nano ZS instrument (Malvern, Worcestershire, UK). In order to measure the agglomerated size of MWCNT sample, their hydrodynamic size was measured with the dynamic light scattering (DLS) technique with the same instrument. Both the zeta potential and the hydrodynamic size were measured in the same dispersion medias that were used for *in vitro* and *in vivo* experiments (Table 3). The DLS technique is suitable for round-shaped particles not fibrous particles. The MWCNT were flexible not rigid, therefore they form agglomerates in three-dimension space. The measured hydrodynamic size gave a rough estimation of the agglomeration degree. SEM images of the lowest (FA04) and highest (FA21) nickel-contaminated MWCNT can be found in Supplementary Figure 1.

### MWCNT suspensions

All nanotubes were weighed and suspended in PBS/7.5% BSA solution (Sigma A8412) as described in Buford et al. (2007). Nanotube suspensions were sonicated for 1 minute in a

cup-horn sonicator (Masonix XL2020) attached to a Forma circulating water-bath at 550 watts and 20 Hz. Stock concentration was 5 mg/ml.

### Animals

C57BL/6 (2-month old) were housed in controlled environmental conditions (22 ± 2°C; 30–40% humidity, 12-h light: 12-h dark cycle) and provided food and water *ad libitum*. All procedures were performed under protocols approved by the IACUC of the University of Montana.

### Alveolar macrophage isolation

Mice were euthanized by sodium pentobarbital (Euthasol™), and the lungs with the heart were removed. Typically, 8–12 mice were lavaged at one time and the lung cells were pooled. This process was repeated several times to establish experimental replicates. Lung lavage was performed using ice-cold PBS (pH 7.4). Lung lavage cells were isolated by centrifugation (400*g*, 5 min, 4°C) and cell counts obtained using a Coulter Z2 particle counter (Beckman Coulter, Brea, CA).

### Cell culture

The cells were suspended in RPMI media supplemented with 10% fetal bovine serum and supplements (0.05 mM 2-mercaptoethanol, sodium pyruvate, and a 100× anti-mycotic/antibiotic cocktail (Mediatech, Manasses, VA)). Cells were suspended at $1 \times 10^6$ cells/ml. A 100 μl sample (100,000 cells) of this was exposed to each MWCNT (at 100 μg/ml or 10 μg/$10^3$ cells or 31.25 μg/$cm^2$ (10 μg on 0.32 $cm^2$)), and experiments were conducted in 96-well plates for 24 h in 37°C water-jacketed $CO_2$ incubators (ThermoForma, Marietta, OH).

### Electron microscopy of alveolar macrophages exposed to MWCNT

Isolated alveolar macrophages (AM) from C57BL/6 mice were exposed to MWCNT at 50 μg/ml for 1 h in suspension culture. The cells were washed once in PBS and resulting macrophage suspensions were fixed in 2.5% EM grade glutaraldehyde in cacodylate buffer at pH 7.2. The cells were then rinsed in $dH_2O$ and resuspended in 1% osmium tetroxide for 1 h and rinsed in $dH_2O$. The cells were dried in a graded ethanol series followed by embedding of the cell pellet in epoxy. Thin sections were stained with 2% uranyl acetate for 30 min at room temperature, rinsed in $dH_2O$, and stained for 5 min with Reynolds lead citrate stain. The cells were imaged in a Hitachi H-7100 transmission electron microscope at 75 kV.

### *In vivo* mouse exposures

All nanoparticles were suspended in dispersion medium (DM, PBS containing 0.6 mg/ml mouse serum albumin and 0.01 mg/ml 1,2-dipalmitoyl-sn-glycero-3-phosphocholine) and sonicated for one minute in a cup-horn sonicator (Masonix XL2020) attached to a Forma circulating water-bath at 550 watts and 20 Hz. Mice were exposed to nanoparticles by oro-pharyngeal aspiration. Briefly, the mice were anesthetized using inhalation isoflurane and a volume of 30 μl of particle suspension (150 μg) was delivered into the back of the throat. By

holding the tongue to the side, the solution was aspirated into the lungs. Mice were euthanized by sodium pentobarbital (Euthasol™).

### Histology

The lungs from each mouse were inflation-fixed through the trachea with 3% paraformaldehyde-PBS and submerged in the same fixative overnight at 4°C. The lungs were washed with cold PBS, dehydrated, and embedded in paraffin. Tissue sections (7 μm) were stained with hematoxylin-eosin (RAS Harris Hematoxylin and Shandon Alcohol Eosin) for histological analysis using a Thermo Shandon automated stainer (Shandon, Pittsburgh, PA).

### Toxicity assay

Cell viability was determined by MTS reagent using the CellTiter$^{96}$ assay (Promega, Madison, WI), according to the manufacturer's protocol. This assay used a colori-metric dye read by a colorimetric plate reader (Molecular Devices, Sunnyvale, CA). In order to avoid distortions in the optical density values steps were taken to remove the MTS reagent (transferring it into another plate for reading) from the cell/particle mixture adhered to the original plate bottom. The formation of bubbles was avoided and the plate was read at 490 nm. Any bubble formation was eliminated by centrifugation before reading.

### Cytokine assays

Mouse IL-1β, and mouse IL-18 DuoSets were obtained from R&D Systems, Minneapolis, MN and ELISA assays performed according to the manufacturer's protocol.

### Microscopy and pathology scoring

Mouse lung tissue sections were imaged at 100× using a Zeiss Axioskop attached to Zeiss digital camera and processed using Zeiss AxioVision software. Two expert observers scored the degree of lung disease visible in the lung sections using a 5-point scale (0, 1, 2, 3, and 4) with zero being no effect and 4 being extreme lung pathology evident. Both scorers were blind to the conditions. Cronbach's-α was used to assess the reliability between observers. Inter-rater reliability was significant at 0.81 indicating agreement between the two observers' scores. There were three exposed mice per MWCNT condition. The values shown in this paper are the median of the two scorers' median value for each condition.

### Fluorescence photomicrographs

Fluorescent confocal photomicrographs of phagolysosomes were obtained in alveolar macrophages (AM) cells stained with acridine orange (1:1000 Calbiochem Cat # KP31322) ± MWCNT for 2 h in culture on 96-well glass-bottom plates (No. 0; MatTek, Ashland, MA). Images were made with an Olympus Fluoview 1000 laser scanning confocal mounted on an inverted IX81 microscope with laser excitation. The processing software was Olympus FV, Version 2.1b. The acridine orange filter uses 488 nm excitation and a 525 nm emission wavelength. All images were at 600×, using a 60× oil objective.

### Statistical analyses

Statistical analyses involved comparison of means using a one-way ANOVA followed by Dunnett's test or Bonferroni's test to compensate for increased type I error. Linear regression analysis was performed to determine possible predictive relationships between variables. The strength of the relationship is expressed as the coefficient of determination ($r^2$), indicating the proportion of variability in *X* explained by *Y*. Statistical significance is a probability of type I error at <5% ($p < 0.05$). The minimum number of experimental replications was 3. Graphics and analyses were performed on PRISM 5.0 and SPSS 18.0.

## Results

### Characterization of nine MWCNT

Two different types of MWCNT were selected for use in this study based on their vendor-specified length and diameter. The different types included: length 1–2 μm and diameter 60–100 nm; length 5–15 μm and diameter 60–100 nm. Each type of material was purchased from leading manufacturers/vendors for evaluation. A total of nine different MWCNT samples were included in the study. The MWCNT were characterized by the Research Triangle Institute as described in Methods section. Table 2 lists the physical characteristics, in addition to purity and major contaminants of the MWCNT. Contaminant levels of iron, nickel, cobalt, and molybdenum are expressed as a percent of the total MWCNT mass. Zeta potential measurements and mean agglomerate size measurements are shown in Table 3. Overall, as expected the zeta potentials were very similar for the nine different MWCNT in the *in vivo* and *in vitro* medias. As expected the agglomerate sizes were all fairly large and varied from 51 to 615 nm in media. Three samples (FA08B, FA10B, and F13) formed large agglomerates ranging from 396 to 615 nm. The other samples had agglomerates ranging from 51 to 295 nm. Most of the short samples had smaller hydrodynamic size.

### Lung pathology from instilled MWCNT (7-day exposure)

C57BL/6 mice were instilled with 150 μg of each MWCNT in order to evaluate any resultant pathology. The dose was selected based on preliminary studies in order to assure visible responses within 7 days. In addition, Porter et al., have shown that lung pathology was essentially maximal within 7 days of exposure (Mercer et al., 2010). Seven days after oro-pharyngeal delivery of the MWCNT the lungs were removed, sectioned and stained. The sections were assessed for pathological anomalies and the lung condition was scored on a 5-point scale from 0 to 4 (least affected to most affected). Figure 1 illustrates the different types of tissue anomalies encountered after 1 week of MWCNT exposure. Figure 1A shows a vehicle control lung. The most typical MWCNT effect is shown in Figure 1B, where cell-associated lesions and increased cellularity around the particles were apparent. Other pathologies include increased cellularity (inflammation) not associated with particles (Figure 1C) and in a few cases, massive particle-associated lesions were apparent throughout the lung section (Figure 1D). All nine MWCNT produced some degree of abnormal lung pathology from mild inflammation to extensive lesion formation. Consistent with the literature, some MWCNT had minimal effects while others had fairly pronounced granulomas (Figure 1D).

In an attempt to understand the differences found in lung inflammation and granulomas produced by the nine MWCNT, we examined the associations of MWCNT metal contaminants to the 7-day lung pathology scores. Figure 2 shows these associations in four scatter-plots (one for each major metal contaminant). Figure 2A clearly shows that nickel contamination is highly associated with 7-day lung pathology reflected in the extremely significant coefficient of determination. Figure 2B shows a moderately significant association with iron contamination, but this is probably the result of influence from two outliers with both high iron and high pathology scores. If these two outliers were removed from the analysis, the regression slope would be a flat line indicative of no association. There was no association with cobalt or molybdenum contamination and 7-day lung pathology (Figures 2C and D, respectively). Taken together, these results indicate that Ni content on the nine different MWCNT was the best predictor of lung pathology.

## Lung pathology is similar for 7- and 56-day exposures

In order to determine whether MWCNT-induced lung pathology at 7 days was persistent over a longer time period, additional MWCNT exposures were conducted with the five 60_100 long particles for 56 days in the same mouse model using the same 150 μg instillation. Note: 50, 100, and 150 μg exposures were also conducted and they all resulted in the same relative degree of long term lung disease (data not shown) suggesting that lung inflammation and pathology peaked at doses of at least 50 μg/ml. Lung sections were assessed as described above and the association between 7- and 56-day pathology scores is shown in Figure 3C. The scores are highly correlated indicating that the MWCNT effects are consistent over time. The pathology scores are lower for the 56-day samples indicating some resolution of inflammation and clearance of particles. Nevertheless, all of the 56-day particle-exposed lungs showed some degree of lung pathology. The average and dispersion of all scoring (7 and 56 day) can be found in Figures 3A and B respectively.

Representative lung sections are shown in Figure 4. Particles, inflammation, and lesions are still present in varying degrees depending on the MWCNT. Furthermore, the nickel content was predictive of the pathological outcome. The higher nickel particles (FA08B, FA17, and FA21) caused more lung tissue anomalies. The low nickel particles (FA04 and FA10B) caused only a small number of lung abnormalities and the particles were apparently cleared easier. Day-7 lung sections for the four 60_100 short MWCNT can be found in Supplementary Figure 2.

## Association of Ni on MWCNT with *in vivo* lung pathology and *in vitro* NLRP3 inflammasome activity

The results shown in Figure 2A provided clear evidence of a significant association between nickel content and pathology score (7-day) in the two 60_100 MWCNT types. This *in vivo* result supported the notion that nickel content is a significant predictor of lung pathology. To determine whether a relevant *in vitro* model of bioactivity (NLRP3 inflammasome activation and/or cell death) was predictive of the *in vivo* potency and nickel content, we exposed C57BL/6 AM to these same MWCNT in 24-h cultures. The results are shown in Figure 5A and B. The release of inflammatory cytokines IL-1β and IL-18 from AM were used as measures of NLRP3 inflammasome activation and both were significantly associated

with the nickel content of the MWCNT (raw data shown in Figure 6A–C). Figure 5C illustrates the extremely signifi-cant association between IL-1β and IL-18 indicating significant collinearity, consistent with the fact that they are the result of the same bioactive process. In contrast, the toxicity in C57BL/6 AM exposed to these nine MWCNT was not associated with nickel content of the particle (Figure 5D). We have determined in other studies with crystalline silica that NLRP3 inflammasome activity is unrelated to cytotoxicity (data not shown). Further evidence of this is shown in Figure 5E as the IL-1β and cell viability is not related. Therefore, the bioactive response, in the form of NLRP3 inflammasome activation in mouse AM exposed to these types of MWCNT, is dependent on the nickel content and this is directly related to the pathological outcome of the particle-exposed lung as described below. It is important to note, however, that MWCNT without any Ni contamination do activate NLRP3, but at a significantly reduced level compared to Ni-contaminated MWCNT (data not shown).

## Association of the C57BL/6 AM NRLP3 inflammasome activation and lung pathology caused by high-nickel MWCNT

To determine whether NLRP3 inflammasome activation was a good predictor of lung pathology, its association with the 7-day lung pathology scores from the mouse exposed lungs was determined and shown in Figure 6. The X-axis in Figure 6A–C is ordered on the basis of nickel content from left (low) to right (high). Both the NLRP3 inflammasome cytokines and the cytotoxicity produced by the MWCNT were good predictors of lung pathology in the C57BL/6 model based on the regression analysis shown in Figure 6D–F. The four MWCNT with the highest nickel content (FA08B, FA11, FA17, and FA21) are the most bioactive, with FA13 being the only outlier (low nickel—high response). Therefore, while cytotoxicity was not associated with the nickel content or NLRP3 inflammasome activation (Figure 5D and E) both cytotoxicity and NLRP3 inflammasome activation was associated with lung pathology.

## High-nickel content in MWCNT causes lysosomal disruption

One potential explanation for the bioactivity of high-nickel MWCNT involves lysosomal disruption leading to cathepsin B release into the cell cytoplasm, NLRP3 inflammasome activation, and subsequent caspase-1 activation, which can occur relatively rapidly (min). To evaluate potential mechanisms, AM morphology and lysosomal structure were examined. Mouse AM cell morphology (transmission electron microscopy) following MWCNT uptake (1-h exposure) can be seen in Figure 7. Normal lysosomal formation is clearly evident for low-nickel MWCNT (FA04 and FA10B) in Figure 7B and D. In addition, the nuclear chromatin is intact and looks similar to the control AM cell nucleus found in Figure 7A. In contrast, high-nickel MWCNT (FA08B, FA17, and FA21) are found free in the cytoplasm (Figures 7C, E, and F) indicating a malformed or ruptured phagolysosome. In addition, the nuclei of AM exposed to high-nickel MWCNT appear much lighter, indicative of chromatin condensation related to potential apoptosis and cell stress.

To examine lysosomal integrity, AM were stained with the lysosomal stain acridine orange and the results are shown in Figure 8. AM stained with acridine orange clearly show intact

phagolysosomes following low-nickel MWCNT exposure (Figure 8A) and a lack of intact phagolysosomes in AM exposed to high-nickel MWCNT (Figure 8B).

### Cathepsin B and caspase-1 inhibitors block cytokine release *in vitro*

Since cathepsin B release from phagolysosomes has been implicated in activating the NLRP3 inflammasome the effect of the cathepsin B inhibitor (10 μM CA-074-Me) on IL-1β and IL-18 release stimulated by one of the highest Ni-contaminated MWCNT (FA21) was examined and shown in Figure 9A and B respectively. FA04 (low Ni contamination MWCNT) was included as a negative control. C57BL/6 AM pretreated (5 min) with the cathepsin B inhibitor CA-074-Me produced significantly less NLRP3 inflammasome cytokines in response to FA21. Similarly, the caspase-1 inhibitor Ac-Tyr-Val-Ala-Asp-CMK (20 μM) significantly blocked cytokine release from AM exposed to FA21. Taken together, these results support the notion that Ni on MWCNT is capable of causing lysosomal disruption, releasing cathepsin B, activating the NLRP3 inflammasome, and in turn activating caspase-1 that cleaves the pro-forms of IL-1β and IL-18 (if available).

## Discussion

There are numerous reports demonstrating that MWCNT can cause lung inflammation, leading to granuloma formation and lung fibrosis. However, the mechanism(s) responsible for the inflammatory response has not been elucidated. MWCNT are prepared using various procedures and catalysts creating a variety of closely related materials varying in diameter, length, alignment, and presence of contaminating metals. There is debate as to what components or characteristics of MWCNT are responsible for the reported biological activity and whether some, or all, of the inflammatory properties are due to metal contaminants on the MWCNT. The purposes of the current study were to use a series of nine well-characterized commercially available MWCNT to (1) determine whether metal contaminants on MWCNT contributed to the biological activity, (2) propose a plausible mechanism of action, and (3) determine whether *in vitro* testing using primary macrophages could be used to predict *in vivo* outcomes. The findings from this study indicate that there are differences in the biological activity of MWCNT from different sources. Furthermore, Ni content on the MWCNT significantly correlated with pathology (Figure 2A) and activation of the NLRP3 inflammasome (Figure 5). In addition, the activation of the NLRP3 inflammasome significantly correlated with pathology (Figure 6) providing a plausible mechanism. The significant and consistent correlation between *in vitro* activation of the NLRP3 inflammasome and pathology supports the notion that *in vitro* screening for particle-induced NLRP3 inflammasome activation could serve as an important tool for studies with other nanomaterials.

Although there was a moderately significant association between iron contamination and pathology (no association was observed for cobalt or molybdenum), this was probably the result of the influence of two outliers that had both high iron and high pathology. The MWCNT tested in this study did not have a linear distribution of iron contamination. It was either extremely high or extremely low, which leaves the question open as to whether iron contamination can cause the effects seen with Ni contamination. It is plausible that

extremely high iron contamination might cause similar bioactivity. In contrast, the association with Ni was highly significant throughout the concentration range. Previous studies support the notion that Ni can be key in inflammation and fibrosis. A study using SWCNT also suggested the importance of Ni in driving an inflammatory response (Liu et al., 2007). NiO has been reported to induce significant lung inflammation (Lu et al., 2009) and NiO nanoparticles cause acute and chronic lung inflammation (fibrosis/granulomatosis) (Cho et al., 2010). In addition, a study using THP-1 cells demonstrated that soluble Ni activated the NLRP3 inflammasome (Caicedo et al., 2009). Phagolysosomes have been reported as sites for ROS formation with redox capable transition metals such as Ni (Pourahmad et al., 2003; McNeilly et al., 2004) and Ni has been reported to contribute to ultra-structural changes in phagolysosomes in macrophages (Murthy & Holovack, 1991). In the present study, MWCNT were shown to cause lysosomal disruption (Figure 8). Therefore, since lysosomal disruption appears to be important in upstream activation of the NLRP3 inflammasome (Tschopp & Schroder, 2010) and correlates well with caspase-1 activation and IL-1β release (Davis & Swanson, 2010), which is consistent with the effects of Ni on macrophages and inflammation, a role of Ni on MWCNT-induced inflammation becomes plausible. The fact that we observed a very high correlation with Ni, in contrast to the other metals present on MWCNT, may suggest that some unique property of Ni may be important in lysosomal disruption and not just ROS production. Since lysosomal integrity has been reported to be dependent on association of LAMP-1 and LAMP-2 with the interior of the lysosomal membrane (Boya & Kroemer, 2008), it can be speculated that Ni may have a strong affinity for these proteins and cause conformational changes upon binding. Nevertheless, while Ni content may be an important contributor to MWCNT-induced inflammation, it is possible that other factors may contribute for other MWCNT or other types of ENM.

In a previous study, using $TiO_2$ nanospheres, short and long $TiO_2$ nanobelts (NB), nanoparticle length was shown to be important in bioactivity (Hamilton et al., 2009). Only the long (>15 micron) NB had significant activity *in vitro* (Hamilton et al., 2009) and *in vivo* (Porter et al., 2012). In the present study, two different lengths of MWCNT were utilized, some were short (1–2 μm) and others generally long (5–15 μm). Although particle length is well known to be important to biological activity and persistence, length may be more important to rigid particles and may not be as important for flexible, tangled MWCNT used in this study (Palomäki et al., 2011). The results from this study suggest that Ni content is one important factor determining the biological activity of MWCNT. When the nanomaterials are rigid and long, similar to asbestos fibres, NLRP3 inflammasome bio-activity can result (Palomäki et al., 2011). The MWCNT used in this study were not rigid and could form complicated three-dimensional structures (aggregates). Other factors such as diameter, aggregation, surface area, contamination, etc., should still be considered as a potential initiator of bioactivity. The results from this study do not suggest that Ni contamination is the only possible initiator of MWCNT bioactivity. Many factors may influence particle uptake that would in turn likely be critical to activation of the NLRP3 inflammasome. Nevertheless, all of the nine different MWCNT were readily taken up *in vitro* by primary murine AM (data not shown).

Activation of the NLRP3 inflammasome by MWCNT is consistent with numerous reports that other particles (e.g. silica, uric acid crystals, asbestos, etc.) that cause inflammation activate the NLRP3 inflammasome (Dostert et al., 2008). In addition, activation of the NLRP3 inflammasome has been reported for other nanoparticles (Yazdi et al., 2010). Consequently, activation of the NLRP3 inflammasome may be an important central event to evaluate in order to determine potential inflammatory activity of any new ENM. The close correlation between the ability of the MWCNT to activate the NLRP3 inflammasome and lung pathology as well as the relationships previously reported linking the NLRP3 inflammasome and lung pathology provide support for using inflammasome activation as an evaluation tool for new ENM. The products of the NLRP3 inflammasome (IL-1β and IL-18) are important regulatory cytokines (Martinon et al., 2009; Dinarello, 2011). Recent studies have shown that blocking IL-1R signaling can reduce pulmonary inflammation and fibrosis (Gasse et al., 2007; Dinarello, 2011). Since both IL-1β and IL-18 are products of the same pathway it explains the close correlation between these two cytokines in this study. In particular, IL-1β has been closely linked to many inflammatory events (Martinon et al., 2009; Arend et al., 2008; Kroeger et al., 2009) and has been shown to be required for the recruitment of PMN after nanoparticle instillation (Yazdi et al., 2010).

Cells most often linked with the NLRP3 inflammasome are tissue macrophages and related cells such as dendritic cells and monocytes (Martinon et al., 2009). Since tissue macrophages such as alveolar macrophages would be the primary innate immune cell to come in contact with inhaled particles it helps explain the close correlation between activation of the NLRP3 inflammasome *in vitro* with the resultant lung pathology. Consequently, *in vitro* assays using primary macrophages or appropriate macrophage cell lines could serve as important screening assay cell culture systems to rapidly screen ENM.

The mechanism to account for MWCNT activation of the NLRP3 inflammasome is shown in Figure 10. Following macrophage uptake of MWCNT into phagolysosomes we propose that Ni on the MWCNT contributes to lysosomal disruption (Figure 8), which has been shown to correlate with caspase-1 activation and IL-1β release (Davis & Swanson, 2010). Lysosomal disruption leads to the release of lysosomal catabolic enzymes, of which cathepsin B has been associated with the formation of the active NLRP3 multimeric protein complex (Tschopp & Schroder, 2010). Consistent with this model, the cathepsin B inhibitor (CA-074 Me) did significantly block IL-1β release (Figure 9). The NLRP3 protein complex recruits and cleaves pro-caspase-1, which in turn cleaves pro-IL-1β and pro-IL-18 into their active forms that can be secreted from macrophages contributing to the subsequent acute inflammatory response (data not shown). This model is also consistent with the report from Liu et al. (2007). In that work the authors provide a model to explain different mechanisms to account for Ni mobilization from SWCNT accounting for its bioactivity (Liu et al., 2007). Various studies have suggested that ROS production could contribute to the bioactivity of nanomaterials, however, Fenoglio et al. (2006) have proposed that MWCNT might be effective ROS scavengers leaving the role of ROS in the mechanism unclear considering the effective inhibition by cathepsin B (Fenoglio et al., 2006). Based on our results, we suggest that the ability of nanomaterials to disrupt the phagolysosome may be the most important

determinant of their inflammatory potential based on the ability of the cathepsin B inhibitor to block IL-1β release (Figure 9).

## Conclusions

Carbon nanotube exposure is becoming a more frequent occurrence in the workplace and through commercially available products. Recent research suggests that some of these materials are bioactive in experimental models consistent with disease initiation. Nanomaterial engineers and producers should be aware of the MWCNT contaminants that coincidentally occur because of the production method. Our research would indicate that high levels of nickel (>2%) on MWCNT, are bioactive in an animal exposure model. Steps should be taken to minimize nickel contamination in addition to other metal contaminants in the MWCNT production process where possible.

## Supplementary Material

Refer to Web version on PubMed Central for supplementary material.

## Acknowledgments

We would like to thank Dr Jim Driver at the University of Montana Electron Microscopy Facility (Division of Biological Sciences), for the EM images of the AM cells and Mr Erik Hill for providing technical assistance. Mr Kevin Trout produced the artwork in Figure 10. The authors are indebted to Dr Nigel Walker and the National Toxicology Program of NIEHS for providing the MWCNT. Furthermore, the authors are indebted to the Research Triangle Institute for the characterization of the MWCNT.

This work was supported by the National Institutes of Health [R01 ES015497 andRC2 ES018742] and COBRE [P20 RR017670].

## References

Arend WP, Palmer G, Gabay C. IL-1, IL-18, and IL-33 families of cytokines. Immunol Rev. 2008; 223:20–38. [PubMed: 18613828]

Bonner JC. Nanoparticles as a potential cause of pleural and interstitial lung disease. Proc Am Thorac Soc. 2010; 7:138–141. [PubMed: 20427587]

Boya P, Kroemer G. Lysosomal membrane permeabilization in cell death. Oncogene. 2008; 27:6434–6451. [PubMed: 18955971]

Buford MC, Hamilton RF Jr, Holian A. A comparison of dispersing media for various engineered carbon nanoparticles. Part Fibre Toxicol. 2007; 4:6. [PubMed: 17655771]

Caicedo MS, Desai R, McAllister K, Reddy A, Jacobs JJ, Hallab NJ. Soluble and particulate Co-Cr-Mo alloy implant metals activate the inflammasome danger signaling pathway in human macrophages: a novel mechanism for implant debris reactivity. J Orthop Res. 2009; 27:847–854. [PubMed: 19105226]

Cassel SL, Joly S, Sutterwala FS. The NLRP3 inflammasome: a sensor of immune danger signals. Semin Immunol. 2009; 21:194–198. [PubMed: 19501527]

Cho WS, Duffin R, Poland CA, Howie SE, MacNee W, Bradley M, Megson IL, Donaldson K. Metal oxide nanoparticles induce unique inflammatory footprints in the lung: important implications for nanoparticle testing. Environ Health Perspect. 2010; 118:1699–1706. [PubMed: 20729176]

Davis MJ, Swanson JA. Technical advance: Caspase-1 activation and IL-1ß release correlate with the degree of lysosome damage, as illustrated by a novel imaging method to quantify phagolysosome damage. J Leukoc Biol. 2010; 88:813–822. [PubMed: 20587739]

Dinarello CA. Blocking interleukin-1ß in acute and chronic autoinflammatory diseases. J Intern Med. 2011; 269:16–28. [PubMed: 21158974]

Dostert C, Pétrilli V, Van Bruggen R, Steele C, Mossman BT, Tschopp J. Innate immune activation through Nalp3 inflammasome sensing of asbestos and silica. Science. 2008; 320:674–677. [PubMed: 18403674]

Drenth JP, van der Meer JW. The inflammasome–a linebacker of innate defense. N Engl J Med. 2006; 355:730–732. [PubMed: 16914711]

Fenoglio I, Tomatis M, Lison D, Muller J, Fonseca A, Nagy JB, Fubini B. Reactivity of carbon nanotubes: free radical generation or scavenging activity? Free Radic Biol Med. 2006; 40:1227–1233. [PubMed: 16545691]

Gasse P, Mary C, Guenon I, Noulin N, Charron S, Schnyder-Candrian S, Schnyder B, Akira S, Quesniaux VF, Lagente V, Ryffel B, Couillin I. IL-1R1/MyD88 signaling and the inflammasome are essential in pulmonary inflammation and fibrosis in mice. J Clin Invest. 2007; 117:3786–3799. [PubMed: 17992263]

Hamilton RF, Wu N, Porter D, Buford M, Wolfarth M, Holian A. Particle length-dependent titanium dioxide nanomaterials toxicity and bioactivity. Part Fibre Toxicol. 2009; 6:35. [PubMed: 20043844]

Johnston HJ, Hutchison GR, Christensen FM, Peters S, Hankin S, Aschberger K, Stone V. A critical review of the biological mechanisms underlying the *in vivo* and *in vitro* toxicity of carbon nanotubes: The contribution of physico-chemical characteristics. Nanotoxicology. 2010; 4:207–246. [PubMed: 20795897]

Kroeger KM, Sullivan BM, Locksley RM. IL-18 and IL-33 elicit Th2 cytokines from basophils via a MyD88- and p38alpha-dependent pathway. J Leukoc Biol. 2009; 86:769–778. [PubMed: 19451398]

Lam CW, James JT, McCluskey R, Arepalli S, Hunter RL. A review of carbon nanotube toxicity and assessment of potential occupational and environmental health risks. Crit Rev Toxicol. 2006; 36:189–217. [PubMed: 16686422]

Lanone S, Boczkowski J. Biomedical applications and potential health risks of nanomaterials: molecular mechanisms. Curr Mol Med. 2006; 6:651–663. [PubMed: 17022735]

Lewinski N, Colvin V, Drezek R. Cytotoxicity of nanoparticles. Small. 2008; 4:26–49. [PubMed: 18165959]

Liang XJ, Chen C, Zhao Y, Jia L, Wang PC. Biopharmaceutics and therapeutic potential of engineered nanomaterials. Curr Drug Metab. 2008; 9:697–709. [PubMed: 18855608]

Liu XY, Gurel V, Morris D, Murray DW, Zhitkovich A, Kane AB, Hurt RH. Bioavailability of nickel in single-wall carbon nanotubes. Advanced Materials. 2007; 19:2790.

Lu S, Duffin R, Poland C, Daly P, Murphy F, Drost E, Macnee W, Stone V, Donaldson K. Efficacy of simple short-term *in vitro* assays for predicting the potential of metal oxide nanoparticles to cause pulmonary inflammation. Environ Health Perspect. 2009; 117:241–247. [PubMed: 19270794]

Martinon F, Mayor A, Tschopp J. The inflammasomes: guardians of the body. Annu Rev Immunol. 2009; 27:229–265. [PubMed: 19302040]

McNeilly JD, Heal MR, Beverland IJ, Howe A, Gibson MD, Hibbs LR, MacNee W, Donaldson K. Soluble transition metals cause the pro-inflammatory effects of welding fumes *in vitro*. Toxicol Appl Pharmacol. 2004; 196:95–107. [PubMed: 15050411]

Mercer RR, Hubbs AF, Scabilloni JF, Wang L, Battelli LA, Schwegler-Berry D, Castranova V, Porter DW. Distribution and persistence of pleural penetrations by multi-walled carbon nanotubes. Part Fibre Toxicol. 2010; 7:28. [PubMed: 20920331]

Murthy RC, Holovack MJ. Ultrastructural changes in rat lungs exposed to combinations of cadmium, zinc, copper, and nickel. J Submicrosc Cytol Pathol. 1991; 23:289–293. [PubMed: 2070354]

Nel A, Xia T, Mädler L, Li N. Toxic potential of materials at the nanolevel. Science. 2006; 311:622–627. [PubMed: 16456071]

Palomäki J, Välimäki E, Sund J, Vippola M, Clausen PA, Jensen KA, Savolainen K, Matikainen S, Alenius H. Long, needle-like carbon nanotubes and asbestos activate the NLRP3 inflammasome through a similar mechanism. ACS Nano. 2011; 5:6861–6870. [PubMed: 21800904]

Poizot P, Laruelle S, Grugeon S, Dupont L, Tarascon JM. Nano-sized transition-metal oxides as negative-electrode materials for lithium-ion batteries. Nature. 2000; 407:496–499. [PubMed: 11028997]

Porter D, Wu N, Hubbs A, Mercer R, Funk K, Meng F, Li J, Wolfarth M, Battelli L, Friend S, Andrew M, Hamilton R, Sriram K, Yang F, Castranova V, Holian A. Differential mouse ulmonary dose- and time course- responses to titanium dioxide nanospheres and nanobelts. Toxicol Sciences. 2012 [E-pub ahead of print].

Pourahmad J, O'Brien PJ, Jokar F, Daraei B. Carcinogenic metal induced sites of reactive oxygen species formation in hepatocytes. Toxicol *In Vitro*. 2003; 17:803–810. [PubMed: 14599481]

Qu GB, Bai YH, Zhang Y, Jia Q, Zhang WD, Yan B. The effect of multiwalled carbon nanotube agglomeration on their accumulation in and damage to organs in mice. Carbon. 2009; 47:2060–2069.

RNCOS. Nanotechnology market forecast to 2013 [Online]. 2009. Available: http://www.rncos.com/report/IM185.htm. Accessed 16 January 2010

Shvedova AA, Kisin ER, Mercer R, Murray AR, Johnson VJ, Potapovich AI, Tyurina YY, Gorelik O, Arepalli S, Schwegler-Berry D, Hubbs AF, Antonini J, Evans DE, Ku BK, Ramsey D, Maynard A, Kagan VE, Castranova V, Baron P. Unusual inflammatory and fibrogenic pulmonary responses to single-walled carbon nanotubes in mice. Am J Physiol Lung Cell Mol Physiol. 2005; 289:L698–L708. [PubMed: 15951334]

Tschopp J, Schroder K. NLRP3 inflammasome activation: The convergence of multiple signalling pathways on ROS production? Nat Rev Immunol. 2010; 10:210–215. [PubMed: 20168318]

Warheit DB, Laurence BR, Reed KL, Roach DH, Reynolds GA, Webb TR. Comparative pulmonary toxicity assessment of single-wall carbon nanotubes in rats. Toxicol Sci. 2004; 77:117–125. [PubMed: 14514968]

Yazdi AS, Guarda G, Riteau N, Drexler SK, Tardivel A, Couillin I, Tschopp J. Nanoparticles activate the NLR pyrin domain containing 3 (Nlrp3) inflammasome and cause pulmonary inflammation through release of IL-1a and IL-1ß. Proc Natl Acad Sci USA. 2010; 107:19449–19454. [PubMed: 20974980]

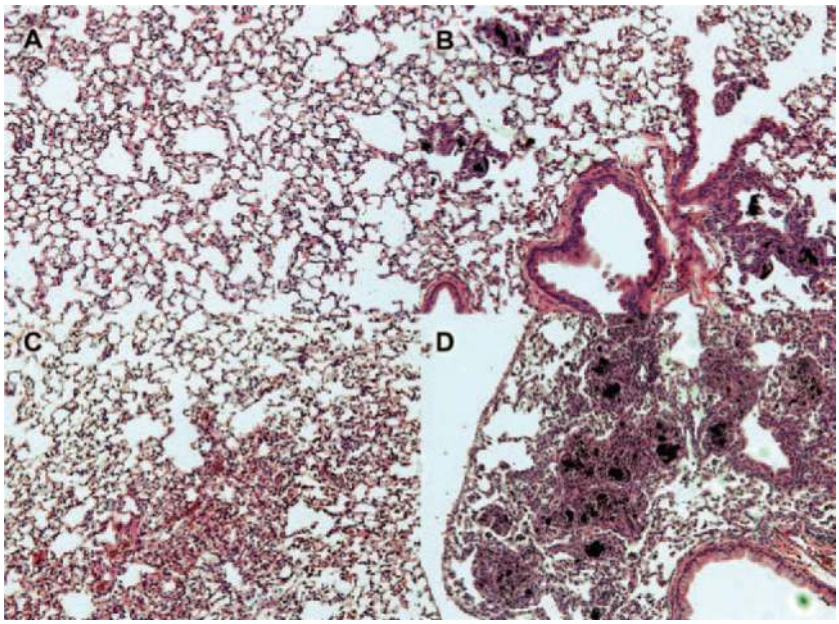


**Figure 1.**

Examples of pathologies observed in C57BL/6 mouse lung sections following 7-day exposure to 150 μg multi-walled carbon nanotubes (MWCNT). (A) Vehicle (DM) control. (B) Most common lung change shown here from 7-day MWCNT exposure (FA05). (C) General inflammation in the absence of particle in a 7-day MWCNT exposed lung section (FA13). (D) Massive inflammation and lesion formation in a 7-day MWCNT (high nickel) exposed mouse lung (FA21). All of the representative photomicrographs were taken at 100× magnification.

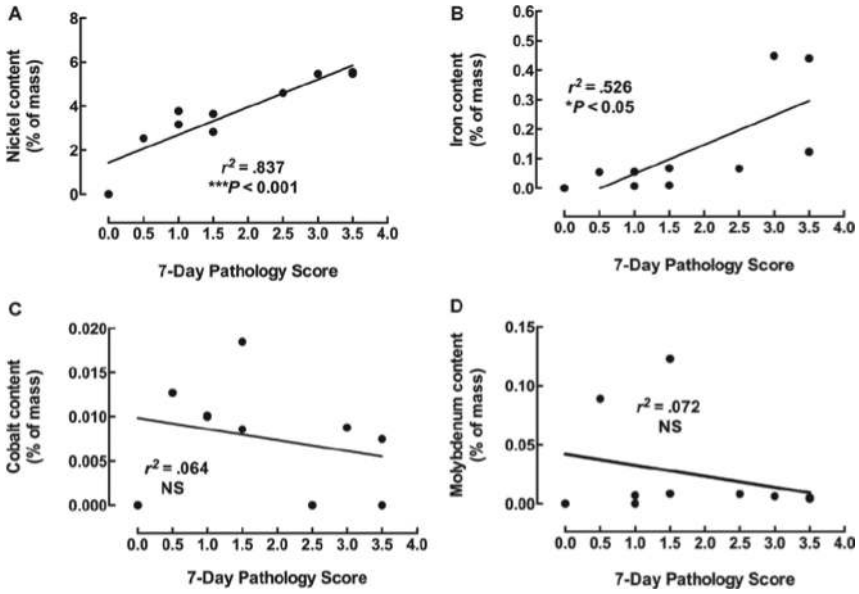


**Figure 2.**

Scatter-plots showing the relationship between 7-day pathology and multi-walled carbon nanotubes (MWCNT) principle metal contents. Relationships between (A) nickel, (B) iron, (C) cobalt, and (D) molybdenum mass on MWCNT and pathology scores. Metal content is expressed as a percent of total mass. Pathology score is the median value of two observers scoring 3 exposed mouse lung samples per MWCNT at 150 μg/mouse. *$p < 0.05$ and ***$p < 0.001$.

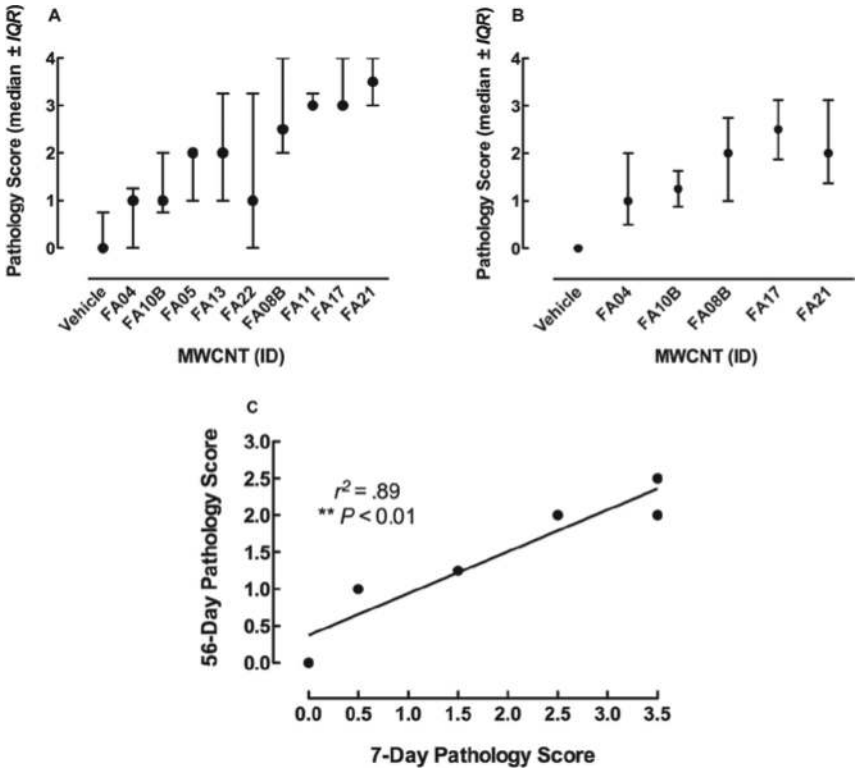


**Figure 3.**

Scatter-plots showing the distribution and variability of pathology scores. (A) Medan ± interquartile range for all pathology scores on scored day 7 samples arranged in order of increasing Ni contamination. (B) Median ± interquartile range for all pathology scores on scored day 56 samples arranged in order of increasing Ni contamination. (C) Correlation between 7- and 56-day scores. The pathology scores after 56 days were obtained by the same two scorers, and the same statistical analyses were conducted as the 7-day scores in Figure 2. Overall, the 56-day scores were generally lower, but there was a significant correlation between the two time points. $^{**}p < 0.01$.

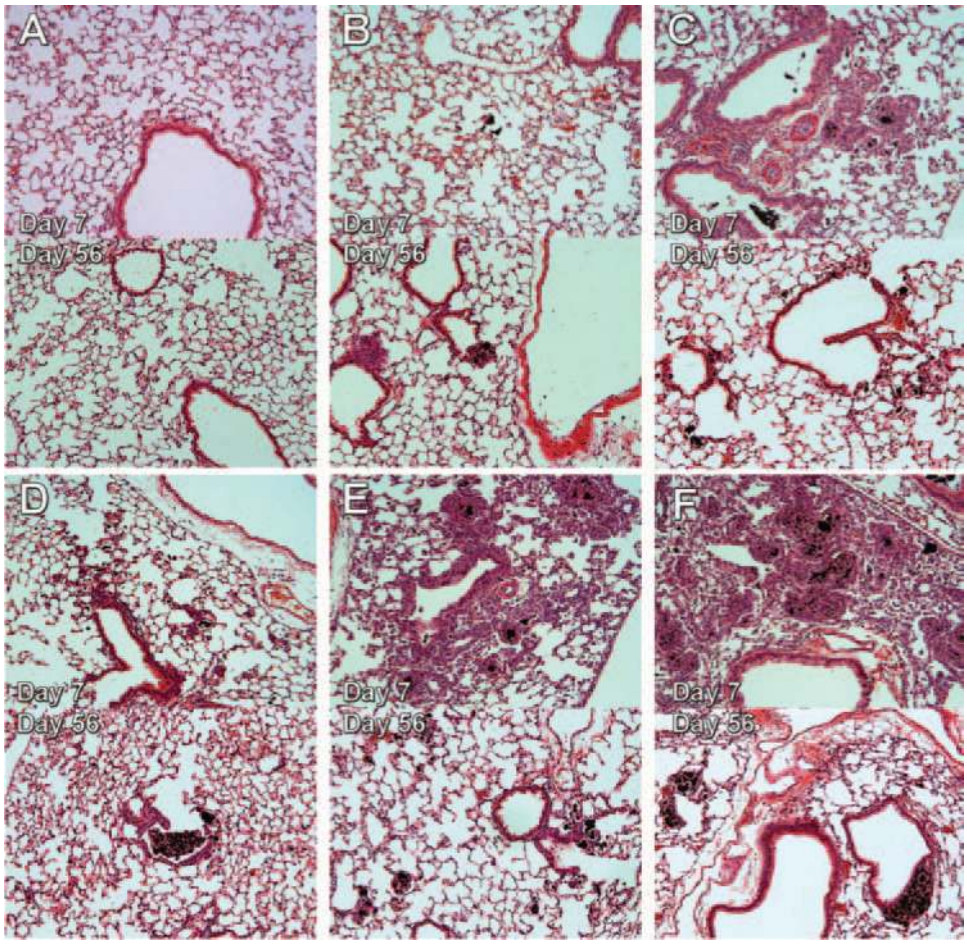


**Figure 4.**

Pathology observed in C57BL/6 mouse lungs following 7 and 56-day exposures to 60_100 long multi-walled carbon nanotubes (MWCNT). C57BL/6 mice were exposed to the 60_100 long MWCNT for 7 days or 56 days and sacrificed. The lungs were processed in the same manner as described in Figure 1 and representative photomicrographs taken. The top panel of the pair is the 7-day exposed lung section and the bottom panel of the pair is the 56-day exposed lung section. (A) Vehicle (DM) control section. (B) FA04 exposure. (C) FA08B exposure. (D) FA10B exposure. (E) FA17 exposure. (F) FA21 exposure. All of the representative photomicrographs were taken at 100× magnification. The 7-day histology for the 60_100 short MWCNT can be found in the Supplementary Figure 1.

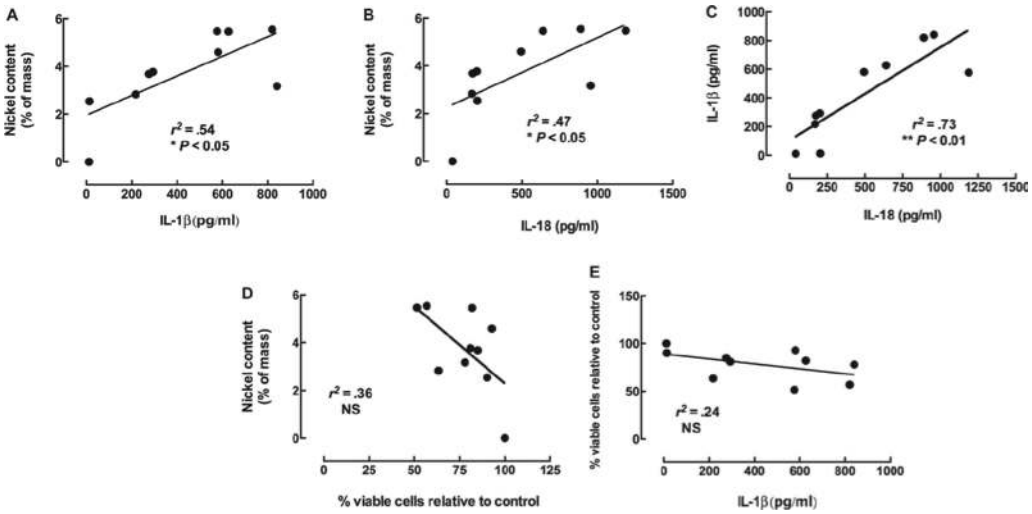


**Figure 5.**

Association between nickel contamination and in vitro measures of multi-walled carbon nanotubes (MWCNT) bioactivity in alveolar macrophages (AM). Freshly isolated C57Bl/6 AM (100 μl at $10^6$ cells/ml) were incubated with 100 μg/ml of the nine MWCNT for 24 h. Measurement of IL-1β and IL-18 required costimulation with 20 ng/ml LPS to generate the pro-forms of the cytokines for the NLRP3 inflammasome-activated caspase-1 to process. (A) The relationship between nickel and IL-1β production in C57BL/6 AM. (B) The relationship between nickel and IL-18 production in C57BL/6 AM. (C) The relationship between IL-1β release and IL-18 release in C57BL/6 AM. (D) The relationship between nickel and cell viability in C57BL/6 AM. (E) The relationship between cell viability and IL-1β release in C57BL/6 AM. $*p < 0.05$, $**p < 0.01$, and $***p < 0.001$ resulting from linear regression analyses.

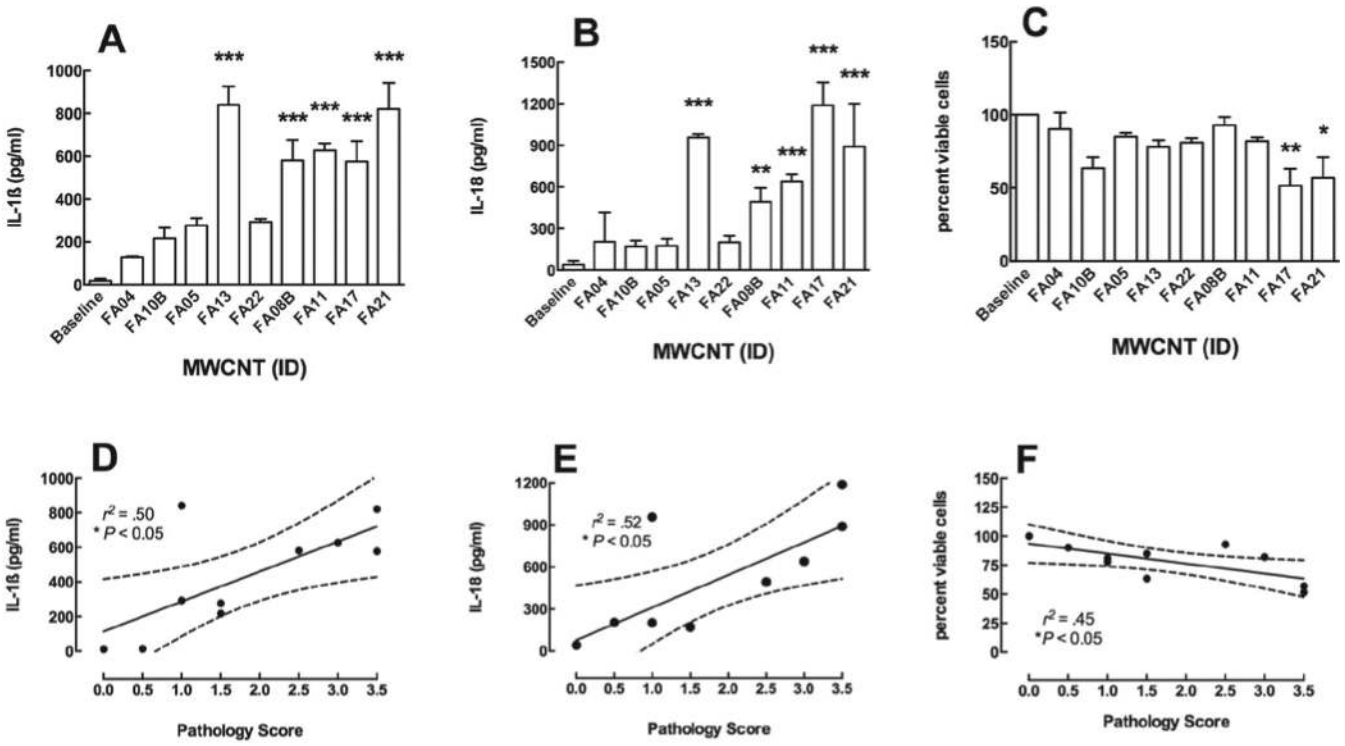


**Figure 6.**

C57BL/6 alveolar macrophages (AM) bioactivity as a predictor of 7-day pathology. (A) Bar graph showing the mean ± SEM IL-1β in response to the 60_100 multi-walled carbon nanotubes (MWCNT) types in order of nickel contamination from low to high. (B) Bar graph showing the mean ± SEM IL-18 in response to the 60_100 MWCNT types in order of nickel contamination from low to high. (C) Bar graph showing the mean ± SEM cell viability in response to the 60_100 MWCNT types in order of nickel contamination from low to high. AM were cultured in 100 μl at $10^6$ cells/ml. (D) Scatterplot showing the relationship between C57BL/6 AM IL-1β production and 7-day pathology score. (E) Scatterplot showing the relationship between C57BL/6 AM IL-18 production and 7-day pathology score. (F) Scatterplot showing the relationship between C57BL/6 AM cell viability and 7-day pathology score. *$p < 0.05$, **$p < 0.01$, and ***$p < 0.001$ compared to baseline or control production levels (A–C) or significant relationship (D–F). Dashed line is the 95% confidence interval (CI).

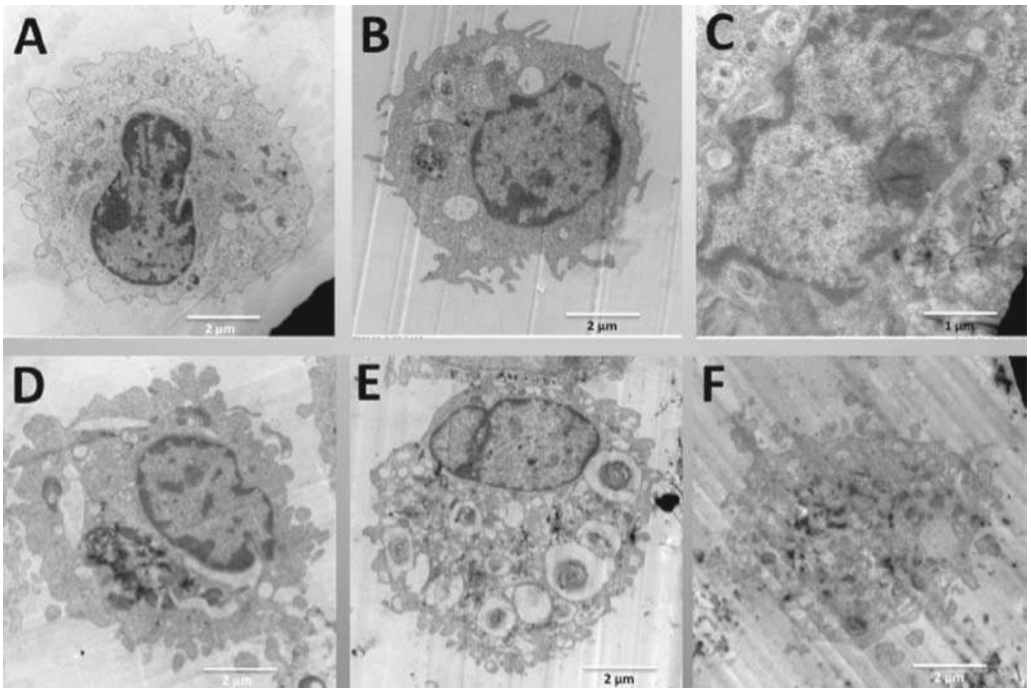


**Figure 7.**

TEM representative images of individual C57BL/6 alveolar macrophages (AM) incubated with the five 60_100 long multi-walled carbon nanotubes (MWCNT). All particle exposures were at 50 µg/ml in 500 µl at $10^6$ cells/ml AM in suspension culture. After 1 h all AM samples were collected, fixed, and processed as described in Methods section for transmission electron microscopy analyses. (A) Control AM with no particle exposure at 7000×. (B) AM exposed to FA04 at 10,000×. (C) AM exposed to FA08B at 15,000×. (D) AM exposed to FA10B at 9000×. (E) AM exposed to FA17 at 7000×. (F) AM exposed to FA21 at 8000×. Lysosomal formation is evident in B and D (low nickel particles), whereas MWCNT free in the cytoplasm are evident in C, E, and F (high nickel particles).

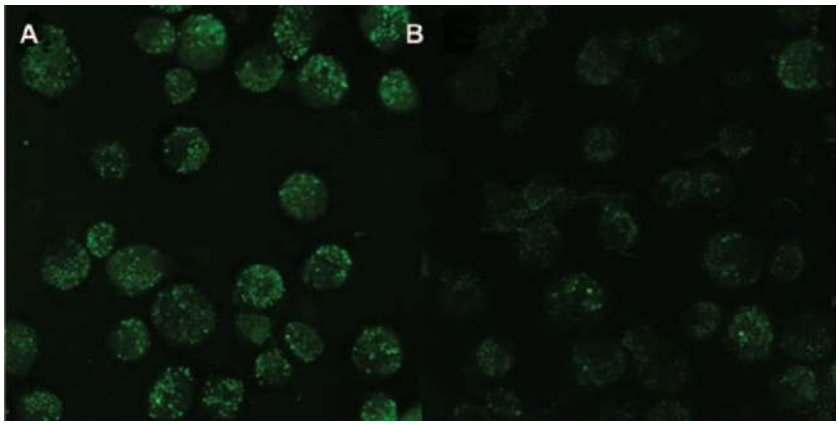


**Figure 8.**

Photomicrographs of alveolar macrophages (AM) stained with acridine orange (lysosomal marker) and exposed to low or high nickel containing multi-walled carbon nanotubes (MWCNT). Freshly isolated AM from C57BL/6 mice were incubated in 96-well glass-bottom plates at 100μl/well of $10^6$ cells/ml with 50 μg/ml of either low nickel (FA04) or high nickel (FA21) MWCNT for 2 h. The cells were co-stained with acridine orange (1:1000) to visualize phagolysosomes and photomicrographs were taken as described in Methods section. (A) Organized lysosomal formation visible in FA04- (low nickel MWCNT) exposed cells. (B) FA21- (high nickel MWCNT) exposed cells show very few phagolysosomes indicated by lack of green stain. All images at 600× using oil immersion objectives.

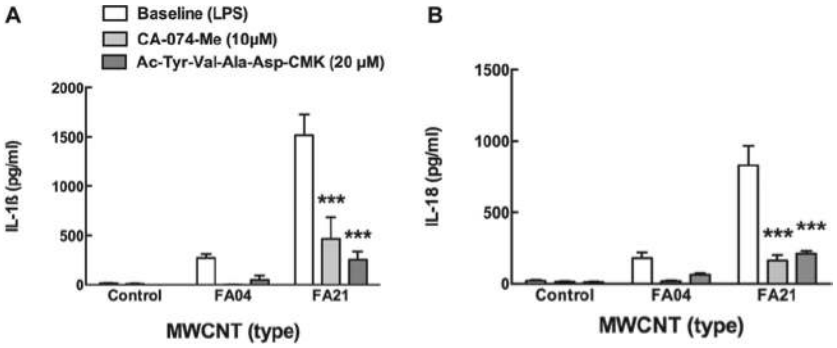


**Figure 9.**

Cathepsin B inhibitor blocks multi-walled carbon nanotubes (MWCNT)-induced NLRP3 inflammasome cytokines production. Freshly isolated alveolar macrophages (AM) from C57BL/6 mice were incubated in 100 μl at $10^6$ cells/ml with 100 μg/ml high nickel (FA21) or low nickel (FA04) MWCNT for 24 h with or without 10 μM cathepsin B inhibitor CA-074-Me or 20 μM caspase 1 inhibitor Ac-Tyr-Val-Ala-Asp-CMK. (A) Bar graph showing the mean ± SEM IL-1β production and (B) bar graph showing the mean ± SEM IL-18 production. ***$p < 0.001$ compared to corresponding baseline condition by Bonferroni's test.

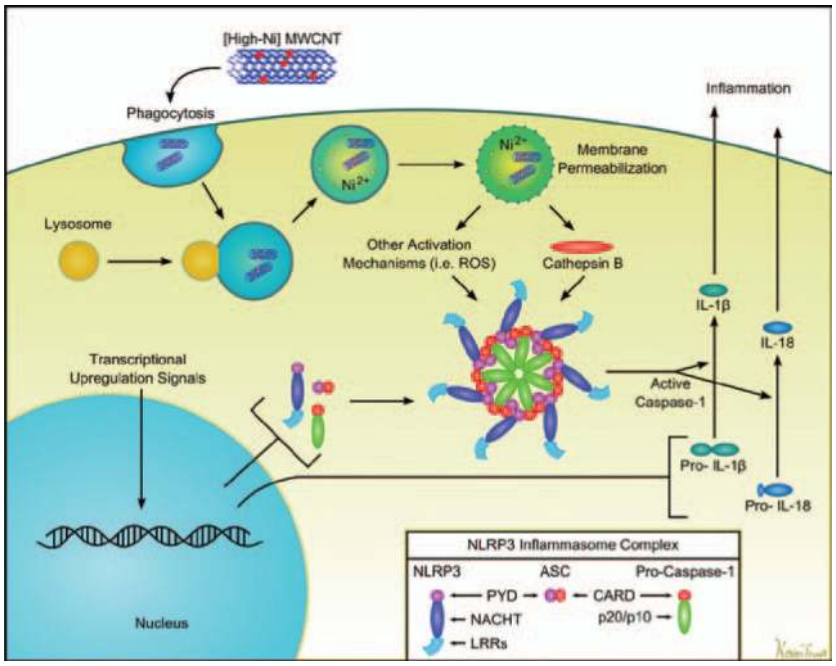


**Figure 10.**

Cell schematic of how nickel-contaminated multi-walled carbon nanotubes (MWCNT) induces the inflammasome leading to inflammatory cytokine release. Two signals are required for IL-1β and IL-18 release. The first is initiated by endocytosis of the contaminated MWCNT. We proposed that when the resulting phagolysosome acidifies, this mobilizes the $Ni^{2+}$ on the MWCNT, which contributes to the rupture of the phagolysosomal membrane. This process then results in the release of cathepsin B into the cytoplasm. Once there, the cathepsin B initiates the assembly of the NLRP3 complex of proteins in combination with ASC and procaspase to form the active caspase ready to cleave the proforms of IL-1β and/or IL-18.

## Table 1

Source location of the nine MWCNT used in this study.

| Vendor | Address | Website |
|---|---|---|
| MK Impex | MK Impex Corp., Mississauga, ON, Canada | www.mknano.com/ |
| Nano Armor | Nanostructured & Amorphous, Materials, Houston, TX, USA | www.nanoarmor.com/ |
| Nano Lab | Nano Lab, Inc., Waltham, MA, USA | www.nano-lab.com/home.html |
| Sigma-Aldrich | Sigma-Aldrich Corp., St Louis, MO, USA | www.sigmaladrich.com/united-states-html |
| Sun Innovations | Sun Innovations, Inc., Fremont, CA, USA | www.nanomaterialstore.com/ |
| Cheap Tubes | Cheap Tubes.com, Brattleboro, VT, USA | cheaptubesinc.com/contact.htm |
| Helix Material | Helix Material Solutions, Inc., Richardson, TX, USA | www.helixmaterial.com/ |

**Table 2**

Physical characterization forthe nine MWCNT samples investigated in this study.

| ID | Chemical name | Vendor | Diam. (nm) | Length (μm) | Purity (%) | Path. index | Fe (%) | Ni (%) | Co (%) | Mo (%) |
|---|---|---|---|---|---|---|---|---|---|---|
| FA08B | 60_100 Long multi-walled carbon nanotube | Aldrich | 24 | 5–15 | 95.3 | 2.5 | 0.0667 | 4.59 | 0 | 0.00805 |
| FA17 | 60_100 Long multi-walled carbon nanotube | Cheap Tubes Inc. | 32 | 5–15 | 94.4 | 3.5 | 0.123 | 5.47 | 0 | 0.0042 |
| FA10B | 60_100 Long Multi-walled carbon nanotube | Nano Amor | 29 | 5–15 | 97 | 1.5 | 0.0678 | 2.83 | 0.0185 | 0.123 |
| FA04 | 60_100 Long multi-walled carbon nanotube | MK Impex Canada | 33 | 5–15 | 97.3 | 0.5 | 0.0543 | 2.54 | 0.0127 | 0.089 |
| FA21 | 60_100 Long multi-walled carbon nanotube | Sun Nano | 27 | 5–15 | 94 | 3.5 | 0.0075 | 5.54 | 0.0075 | 0.00505 |
| FA13 | 60_100 Short multi-walled carbon nanotube | Helix Material Solutions | 34 | 1–2 | 96.8 | 1.0 | 0.0553 | 3.17 | 0.0101 | 0 |
| FA05 | 60_100 Short multi-walled carbon nanotube | MK Impex Canada | 29 | 1–2 | 96.3 | 1.5 | 0.00971 | 3.65 | 0.00857 | 0.0083 |
| FA22 | 60_100 Short multi-walled carbon nanotube | Sun Nano | 39 | 1–2 | 96.3 | 1.0 | 0.0073 | 3.77 | 0.01 | 0.00685 |
| FA11 | 60_100 Short multi-walled carbon nanotube | Nano Amor | 45 | 1–2 | 94.1 | 3.0 | 0.449 | 5.46 | 0.00878 | 0.0061 |

## Table 3

Zeta potential and average agglomeration size for all MWCNT in water, dispersion media (DM), and culture media (RPMI).

| Sample name & media | Zeta potential (mV) | Size (nm) | Sample name & media | Zeta potential (mV) | Size (nm) | Sample name & media | Zeta potential (mV) | Size (nm) |
|---|---|---|---|---|---|---|---|---|
| FA04 in H2O | –17.3 | 675 | FA04 in DM | –7.69 | 102, and 644 | FA04 in RPMI | –11.3 | 294 |
| FA05 in H2O | 3.55 | 459 | FA05 in DM | –14.2 | 283 | FA05 in RPMI | –11.9 | 225 |
| FA08B in H2O | –16.5 | 632 | FA08B in DM | –11.5 | 400 | FA08B in RPMI | –11.6 | 396 |
| FA10B in H2O | –20.8 | 342 | FA10B in DM | –18.7 | 405 | FA10B in RPMI | –12.4 | 122, 295, and 615 |
| FA11 in H2O | 15.7 | 395 | FA11 in DM | –10.7 | 132 | FA11 in RPMI | –10.9 | 51 and 220 |
| FA13 in H2O | –20.3 | 531 | FA13 in DM | –10.6 | 416 | FA13 in RPMI | –12.4 | 122 and 396 |
| FA17 in H2O | 13.0 | 560 | FA17 in DM | –9.72 | 332 | FA17 in RPMI | –11.0 | 68 and 220 |
| FA21 in H2O | –17.2 | 712 | FA21 in DM | –8.16 | 469 | FA21 in RPMI | –12.0 | 122 and 295 |
| FA22 in H2O | 24.3 | 396 | FA22 in DM | –6.87 | 273 | FA22 in RPMI | –12.8 | 170 |
| H2O | n/a | n/a | DM vehicle | 36, 1.53, and –46.3 | 3.4 and 106 | RPMI | n/a | 7 and 48 |